Editors' Suggestion

Bright Chiral Single-Photon Emission Underpinned by Independent Tailoring of Q and V

Kai Liu,[1,2] Qi-hang Zhang,[1,3,4,5] Zi-hao Dong,[1,3,4,5] Zhi-xiang Li,[1,3,4,5] Chao Zhang,[1,3,4,5] Shao-jie Fu,[1,2] Xu-hao Hong,[1,2]
Yan-qing Lu,[1,3,4,5,*] Yan-feng Chen,[1,3,4,5,†] Jun Du,[1,2,‡] Xue-jin Zhang,[1,3,4,5,§] and Yong-yuan Zhu[1,2]
[1]*National Laboratory of Solid State Microstructures, and Collaborative Innovation Center of Advanced Microstructures, Nanjing University, Nanjing, 210093, China*
[2]*School of Physics, Nanjing University, Nanjing, 210093, China*
[3]*Key Laboratory of Intelligent Optical Sensing and Manipulation, Nanjing University, Nanjing, 210093, China*
[4]*Jiangsu Key Laboratory of Artificial Functional Materials, Nanjing University, Nanjing, 210093, China*
[5]*College of Engineering and Applied Sciences, Nanjing University, Nanjing, 210093, China*

(Received 5 September 2025; revised 14 November 2025; accepted 23 December 2025; published 10 February 2026)

The construction of cavity quantum electrodynamic systems is pivotal for advancing the development of quantum emitters, yet it is fundamentally constrained by the trade-off between a cavity's quality factor (Q) and its mode volume (V) in conventional cavities. This causes a bottleneck for single-photon sources when improving the key performance metrics of brightness, purity, and indistinguishability. Here, we overcome this limitation by invoking nonradiative states in the plasmonic metasurface that decouples Q and V. Quasibound states in the continuum regulate electromagnetic field confinement in time (Q) while anapole states enable strong electromagnetic field confinement in space (V). This independent manipulation over Q and V allows us to separately control Purcell factor and cavity linewidth, leading to concurrent improvements of brightness and indistinguishability. Working at room temperature, single-photon emission from two-dimensional hexagonal boron nitride integrated with the plasmonic metasurface is raised by about 3 orders of magnitude. Furthermore, maximal chiral emission is also demonstrated via coordinated spatiotemporal regulation. Our findings pave the way for practical application of compact quantum emitters, and provide new insights into light-matter interaction.

DOI: 10.1103/kf83-1b8s

Introduction—The single-photon emitter is a crucial elementary block for quantum information processing [1,2]. Bright, high-purity, and indistinguishable single-photon emitters have been pursued since the birth of quantum science and technology. Among a variety of materials as single-photon emitters [3–8], two-dimensional (2D) layered hexagonal boron nitride (h-BN) with atomic defect [9] is regarded as a promising candidate for practical quantum sources. The short excited-state lifetimes (~1–3 ns [10]), high quantum efficiency (>80% [11]), and high Debye-Waller factor (~70% [12]), manifest h-BN one of the brightest single-photon emitters at room temperature. Additionally, h-BN's low optical loss [13] and layered structure allow for easy exfoliation and integration into compact photonic devices [14–17].

Despite these advantages, h-BN single-photon emitters face inherent limitations such as fixed nanosecond-scale lifetimes and trivial polarization feature. Coupling single-photon emitters with cavities [18–21] is a well-established strategy to enhance light-matter interaction by modifying the local density of optical states [22]. The efficacy of this enhancement can usually be quantified by the Purcell factor, which is proportional to the ratio of the cavity's quality factor (Q) to its mode volume (V). Whereas, a fundamental challenge arises from the inherent interdependence of Q and V in conventional cavity platforms. On one hand, dielectric structures can achieve very high Q due to low material absorption, but their V is constrained by the diffraction limit. On the other hand, plasmonic cavities can concentrate light into deep-subwavelength V, but the intrinsic Ohmic losses of metals result in low Q. Some solutions leverage metal-insulator-metal (MIM) structures by shrinking the gap size to further compress V down to the picoscale [23]. However, this gives rise to issues such as fabrication complexity, spatial misalignment, and quantum tunneling effects [24]. This deeply rooted trade-off between Q and V imposes a severe bottleneck on the maximum achievable light-matter interaction strength, and resists the concurrent elevation of brightness and indistinguishability, where both large Purcell factor and low Q are required [25].

Overcoming this fundamental limitation requires a paradigm shift in cavity design, moving towards constructions that allow for the independent tailoring of V and Q. Recently, the collaboration of anapole states [26] and

---

[*] Contact author: yqlu@nju.edu.cn
[†] Contact author: yfchen@nju.edu.cn
[‡] Contact author: jdu@nju.edu.cn
[§] Contact author: xuejinzh@nju.edu.cn

© 2026 American Physical Society

quasibound states in the continuum [27] (quasi-BICs) has witnessed immense field enhancement breaking free from the constraints [28]. Unlike conventional approaches, anapole states arising from destructive interference between Cartesian electric dipole (ED) and toroidal dipole (TD) enable compressed V and strong near-field enhancement [26,29] through higher-order multipoles. And quasi-BICs provide a pathway for precise control over radiative loss, allowing for systematic optimization of Q to achieve maximum field enhancement [30–32]. By synergistically combining these two physical mechanisms, the optimization of Q and V can be effectively decoupled, breaking the traditional trade-off and unlocking a new regime of light-matter interaction. These nonradiative states also exhibit unique polarization properties which demonstrate quantized orbital angular momentum [33] or maximal chirality [34,35].

Here, we place defective 2D h-BN onto a plasmonic cavity array with open free space to make hotspots and single-photon emitters readily adjoin each other, supporting anapole states and quasi-BICs. It is the high-order electromagnetic (EM) multipole instead of prevailing ED that underlies the tremendous field enhancement at hotspots. From the perspective of Fermi's golden rule [36], our proposed architecture is also advantageous for overlapping dipole moment and local electric field, and providing considerable plasmonic mode density in the wake of localized modes with near-zero group velocity. The structural asymmetry regulates the quasi-BICs to manifest maximum electric field intensity. Maximal intrinsic chirality can be obtained by manipulating mirror asymmetry along in-plane direction, where BICs are formed for a specific circular polarization.

Results and discussion—In our design, the 2D defective h-BN is coupled with cruciform-structured plasmonic metasurface, as shown in Fig. 1(a). To suppress Ohmic loss, the cruciform structure is etched on single-crystalline Ag (Secs. 1 and 2 of Supplemental Material [37]) grown in a liquid environment [50]. As shown in the inset in Fig. 1(a), the unit cell of the metasurface consists of two orthogonal grooves with the same gap size (w) and etching depth (h). The horizontal groove crosses through the period, and the vertical groove has a length of L. The sharp corners close to each other construct a MIM structure [51] and support gap plasmon polariton (GPP) mode under x-polarized input light. The opposite magnetic field on the two ends of the grooves constructs a magnetic loop and forms a TD moment in the center, which can destructively interfere with ED and result in anapole states (Appendix A).

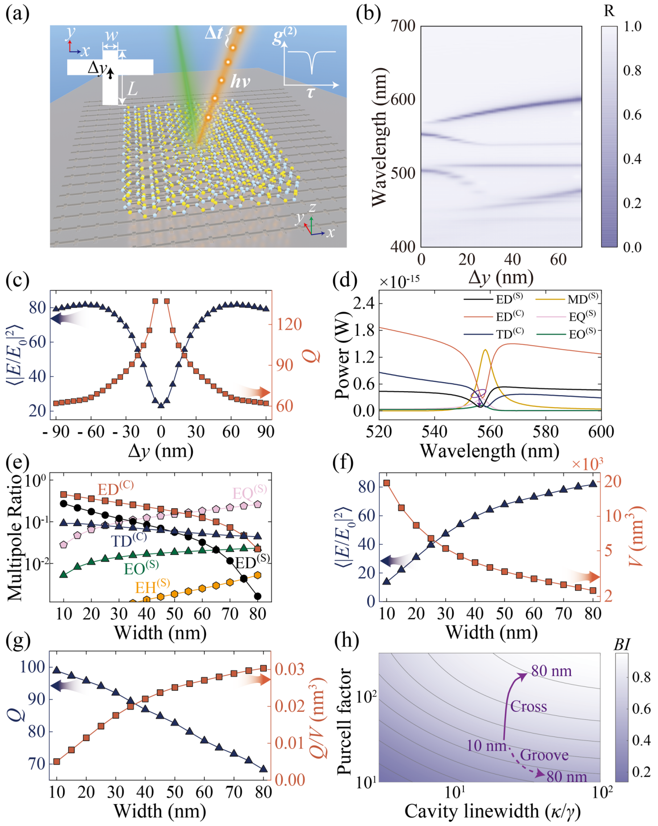

FIG. 1. h-BN coupled with plasmonic metasurface. (a) Schematic of the 2D defective h-BN coupled with plasmonic metasurface. (b) Calculated reflection spectra with Δy, in which $L = 100$, $h = 30$, $w = 40$ nm, and the array period is optimized as $P = 400$ nm (Sec. 3 of Supplemental Material [37]). The thickness of h-BN is set as 25 nm. (c) Calculated Q and average field enhancement ($w = 80$ nm). (d) Multipole decomposition spectra of the quasi-BIC in Cartesian (C) and spherical (S) coordinates. MD: magnetic dipole. (e) Multipole ratio of the quasi-BICs with optimal Δy values, i.e., $\gamma_{\rm rad} = \gamma_{\rm diss}$. EH: electric hexadecapole. (f) Calculated average field enhancement and effective mode volume V of the quasi-BICs with optimal Δy values. (g) Calculated Qs and corresponding Q/V ratios of the quasi-BICs with optimal Δy values. (h) Calculated contour map of the product of brightness and indistinguishability, plotted as function of cavity linewidth (κ) and Purcell factor. The pure dephasing rate is chosen as a fixed value of $\gamma^* = 10\gamma$, where γ is the population decay rate of the emitter. The uncoupled emission $Q\,[\propto 1/(\gamma + \gamma^*)]$ of the emitter is estimated as ~198 according to Appendix B.

The reflection spectra with structural asymmetry (Δy) is shown in Fig. 1(b). At the high symmetry point of the cruciform structure ($\Delta y = 0$), a radiative GPP mode and a nonradiative BIC with zero linewidth are supported. With the increase of Δy, two modes gradually split up in the frequency domain. As shown in Fig. 1(c), the Q of the long-wavelength mode decreases with Δy, which provides pathways to regulate the radiative loss. With the change of structural asymmetry, the local field enhancement is modulated by the varying radiative loss, which can be expressed as [52,53]: $|E_\omega/E_0|^2 \propto \gamma_{\rm rad}/[V(\gamma_{\rm rad} + \gamma_{\rm diss})^2]$, where E_ω and E_0 denote the enhanced electric field and the input electric field, V is the effective mode volume, and $\gamma_{\rm rad}$ and $\gamma_{\rm diss}$ represent the radiative and dissipative losses of the system. The right-hand side of the formula is exactly proportional to the emission enhancement factor ($\mathrm{EF_{em}}$), which is the product of Purcell factor [$\propto Q/V \propto 1/V(\gamma_{\mathrm{rad}}+\gamma_{\mathrm{diss}})$] and cavity quantum efficiency [$\gamma_{\mathrm{rad}}/(\gamma_{\mathrm{rad}}+\gamma_{\mathrm{diss}})$] (details can be found in Sec. 4 of Supplemental Material [37]). The local field intensity and emission enhancement reaches maximum when the system loss is tuned by the Δy value to satisfy $\gamma_{\mathrm{rad}} = \gamma_{\mathrm{diss}}$ condition (i.e., cavity quantum efficiency ~50%), consistent with the maxima in Fig. 1(c).

On the other hand, the multipole component [54,55] (Sec. 5 of Supplemental Material [37]) ratio directly impacts V. Near the resonant region [Fig. 1(d)], Cartesian ED and TD moments destructively interfere with each other (i.e., anapole states), while higher-order multipoles such as electric quadrupole (EQ) and electric octupole (EO) begin to emerge and dominant the radiation, which leads to unconventional modulation on V. In cruciform structure, quasi-BICs can be tuned to satisfy the $\gamma_{\mathrm{rad}} = \gamma_{\mathrm{diss}}$ condition, thus the field enhancement $|E_\omega/E_0|^2 \propto \gamma_{\mathrm{rad}}/[V(\gamma_{\mathrm{rad}}+\gamma_{\mathrm{diss}})^2]$ is reduced to $|E_\omega/E_0|^2 \propto 1/(V\gamma_{\mathrm{rad}})$. $1/\gamma_{\mathrm{rad}}$ is proportional to the radiated power, which can be decomposed into multipole series [28,56]:

$$\left|\frac{E_\omega}{E_0}\right|^2 \propto \frac{1}{V\gamma_{\mathrm{rad}}} \propto \frac{P_{\mathrm{rad}}}{V} = \frac{P_{\mathrm{rad}}^{\mathrm{ED}}}{V_{\mathrm{ED}}} + \frac{P_{\mathrm{rad}}^{\mathrm{EQ}}}{V_{\mathrm{EQ}}} + \frac{P_{\mathrm{rad}}^{\mathrm{EO}}}{V_{\mathrm{EO}}} + \ldots,$$

where P_{rad} is the total radiated power, $P_{\mathrm{rad}}^{\mathrm{ED}}, P_{\mathrm{rad}}^{\mathrm{EQ}}, P_{\mathrm{rad}}^{\mathrm{EO}}, \ldots$ are the power radiated into the form of multipole component, and $V_{\mathrm{ED}}, V_{\mathrm{EQ}}, V_{\mathrm{EO}}, \ldots$ are corresponding volume-related quantities. Former research results show that higher-order multipole components exhibit smaller volume [56]: $V_{\mathrm{ED}} > V_{\mathrm{EQ}} > V_{\mathrm{EO}} > \ldots$. For cruciform structure, the magnitude of ED and TD moment can get even closer with the increase of w, form better elimination and provide higher ratio of higher-order multipoles [Fig. 1(e)], which is thus related to smaller V and higher field enhancement [Fig. 1(f)]. As higher-order multipoles invoked, achieving large enhancement no longer requires an extremely narrow gap. This phenomenon differs fundamentally from conventional dimer or nanoparticle-on-mirror systems. In those paradigms, ED dominates the radiation and extremely small gaps are required to compress V_{ED} down to the level of $\sim 10^{-10}$ cubic wavelength, as often demanded in picocavity schemes.

While the cavity loss increases with the gap width, the independent manipulation by anapole states enables more pronounced compression of V, which still enhances the Purcell factor ($\propto Q/V$) [Fig. 1(g)]. The comprehensive performance metric, defined as the product of brightness and indistinguishability (Sec. 6 of Supplemental Material [37]), is plotted in Fig. 1(h). Optimal product values cluster in the upper-right region, corresponding to configurations with broad cavity linewidths (low Qs) and enhanced Purcell factors. As the gap width increases from 10 to 80 nm, the changing trend of cavity linewidth and Purcell factor is marked by the solid arrow in Fig. 1(h), which means our system simultaneously achieves Purcell factor enhancement and Q reduction, resulting in ~1.5-fold improvement of the overall product of brightness and indistinguishability. To make a comparison, the situation for a single groove structure (with same structural parameters as the vertical groove of the cruciform structure) is marked by the dashed arrow in Fig. 1(h). For this conventional ED-based MIM system, the decrease of Q leads to the decrease of Purcell factor, which will fall into a trade-off relation between brightness and indistinguishability.

In experiment, few-layer 2D h-BNs with different thickness are prepared by mechanical exfoliation on $\mathrm{SiO_2/Si}$ substrate. The exfoliated h-BN samples are then disposed with reactive ion etching (RIE) and annealed at 800 °C in an Ar atmosphere for 2 h, which generates carbon-related visible-range defect [9] in h-BN.

The metasurface is fabricated by focused ion beam (FIB) with the parameters of $w = 80$ and $\Delta y = 60$ nm, which corresponds with the maximum theoretical field enhancement in Fig. 1(c). Then the h-BN sample is transferred to couple with the metasurface by dry-transfer method. The h-BN sample, the fabricated metasurface, and the integrated system are characterized in Appendix B (far field) and Sec. 7 of Supplemental Material [37] (near field), which shows good consistency between theory and experiment.

The single-photon emission from the integrated system is then mapped, and the strongest emission spectra are shown in Fig. 2(a). Owing to the collaboration of anapole states and quasi-BICs, the single-photon emission from the hybrid sample is enhanced by ~90 folds compared to that on $\mathrm{SiO_2/Si}$ substrate, in the same order of magnitude with calculated field intensity enhancement in Fig. 1(c). And the emission linewidth is significantly broadened [Fig. 2(a) inset], indicating rapid cavity decay rate which outpaces pure dephasing process and improves indistinguishability.

The time correlation measurement with Hanbury Brown–Twiss setup (Sec. 8 of Supplemental Material [37]) is carried out to confirm the quantum feature of the coupled structure. The measured second-order correlation function [$g^{(2)}(\tau)$] with uncertainties is shown in Fig. 2(b). To demonstrate the bunching effect over long timescales and the antibunching effect near zero time delay, a symmetric log scale is employed, with linear region between −5 and 5 ns and logarithmic scaling elsewhere. A $g^{(2)}(0)$ value of 0.386 is given by the three-level model fitting [red line in Fig. 2(b)]: $g^{(2)}(\tau) = 1 - a\exp(-|\tau|/\tau_a) + b\exp(-|\tau|/\tau_b)$, where $a = 0.652$ is the antibunching strength, $\tau_a = 0.856$ ns is the antibunching lifetime, $b = 0.038$ is the bunching strength, and $\tau_b = 4.45$ μs is the bunching lifetime. The fitting results show that bunching effect ($b = 0.038$) is minor and does not challenge the single-photon nature of the emitter. Following the standardized correction tutorial [57], the influence of background fluorescence and detector timing jitter is accounted (Sec. 9 of Supplemental Material

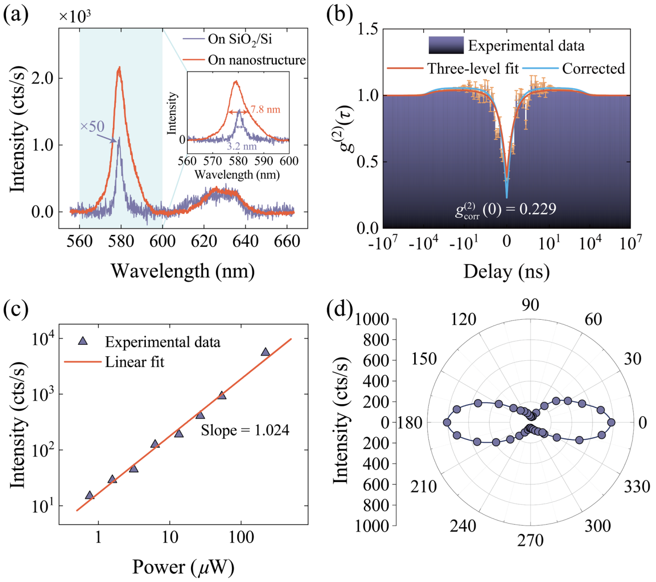

FIG. 2. Far-field characteristics of the fabricated samples. (a) Emission spectra of the coupled structure. The shaded area is enlarged in the inset. (b) Measured $g^{(2)}(\tau)$ data and uncertainties (error bars) with a symmetric log scale. (c) Input power dependency of the single-photon emission from the hybrid sample. (d) Polarization dependency of the single-photon emission from the hybrid sample.

[37]), which yields a corrected true $g^{(2)}_{\mathrm{corr}}(0)$ value of 0.229 [blue line in Fig. 2(b)], well below the single-photon criterion of 0.5.

Figure 2(c) shows the input power dependency of the single-photon emission from the coupled structures. The slope of the fitted curve of 1.024, i.e., linear dependency on input power, is consistent with the feature of photoluminescence. The polarization characteristics of the single-photon emission are shown in Fig. 2(d). With x-polarized input laser, the emitted signal is collected when the azimuth angle of the polarization plate (placed between the long-pass filter and the detector) rotates from 0° to 360°. A typical fusiform pattern is obtained, compatible with the polarization character of the metasurface.

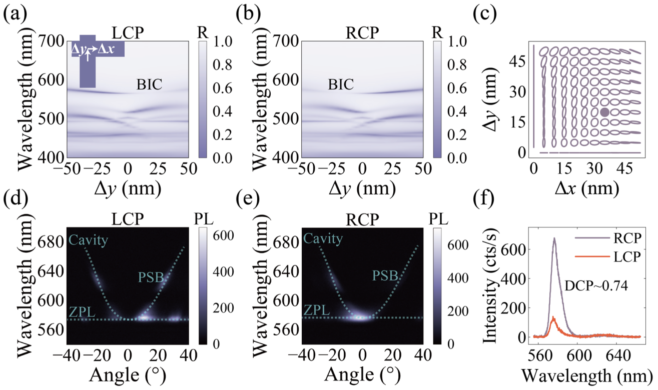

FIG. 3. Chiral single-photon emission. (a),(b) Calculated reflection spectra for the LCP (a) and RCP (b). The parameters are $L_1 = 300$, $L = 200$, $w = 160$, $h = 60$, $P = 400$, and $\Delta x = 35$ nm. (c) Eigenpolarization map with structural asymmetry. (d),(e) Angle-resolved single-photon emission spectra for the LCP (d) and RCP (e). (f) Single-photon emission spectra for the LCP and RCP at Γ point.

The cruciform structure can also effectively address the inherent linear polarization limitation of defects in h-BN. By simply breaking the mirror symmetry along orthogonal direction, the same independent manipulation over Q and V allows to selectively enhance specific circular polarization. In this chiral configuration, the length of the horizontal groove is adjusted to a finite value of $L_1 = 300$ nm to break mirror symmetry. To suppress V, the gap width is chosen as a large value of $w = 160$ nm. After shifting the horizontal groove the distance of Δx from the origin [Fig. 3(a) inset], the mirror symmetry is broken, and the BIC point for left-handed circular polarization (LCP) [Fig. 3(a)] and right-handed circular polarization (RCP) [Fig. 3(b)] offsets from $\Delta y = 0$ in the opposite direction. In this case, the BIC point for one specific circular polarization is the quasi-BIC one for the other circular polarization. Under proper combination of $\Delta x = 35$ and $\Delta y = 20$ nm, Q is tuned to selectively enhance one circular polarization, where the quasi-BIC can satisfy the $\gamma_{\mathrm{rad}} = \gamma_{\mathrm{diss}}$ condition which manifests the strongest response, leading to maximal chirality. The eigenpolarization map is shown in Fig. 3(c), complete circularly polarized far-field radiation also occurs at $\Delta x = 35$ and $\Delta y = 20$ nm, coinciding with the quasi-BIC condition.

The chiral metasurface is fabricated by FIB with $\Delta x = 35$ and $\Delta y = 20$ nm. The metasurface is characterized by angle-resolved white-light reflection spectra in Appendix C, where the accuracy of our theory is confirmed. From theoretical results shown in Sec. 10 of Supplemental Material [37] and Appendix C, strong chirality can be observed at the Γ point, in which the circular dichroism (CD) is 0.98 and the degree of circular polarization (DCP) of emission is 0.83. Experimentally, the hybrid system of h-BN and metasurface is excited with linearly polarized 532 nm laser, and the emitted LCP and RCP signals are collected. The single-photon emission couples with cavity mode at the Γ point, as shown in Figs. 3(d) and 3(e). For the LCP, the emission couples with the BIC and the intensity is suppressed by the nonradiative state. In contrast, the emission couples with the quasi-BIC for the RCP, thus the single-photon emission is greatly enhanced. In total, the angle-resolved photoluminescence spectra [Figs. 3(d) and 3(e)] align well with the white-light reflection spectra in Appendix C. And according to the single-photon emission spectra at Γ point in Fig. 3(f), the zero phonon line (ZPL) is greatly enhanced compared with the phonon sideband (PSB) because of the coupling with cavity mode at the Γ point, in which a large experimental DCP of ∼0.74 is obtained.

The EF of single-photon emission hinges on the thickness of the h-BN on account of evanescent EM wave mode. RIE disposes the sample from top to bottom, and the atomic

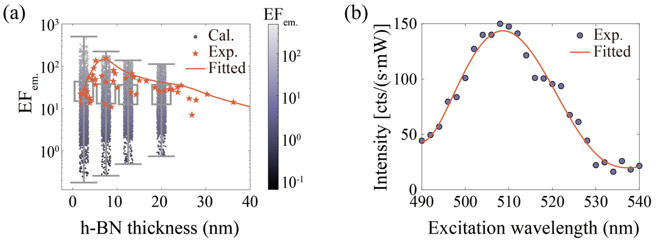

FIG. 4. Additional enhancement. (a) Calculated and experimental EF_{em} with the thickness of h-BN. The calculated results are randomly shifted in horizontal direction for clarification. Lines in error bars represent values of minimum and maximum, and square markers represent the mean values. In experiment, 532 nm continuous-wave laser is used to excite the samples. The curve is fitted with the maximum experimental data of different thickness. (b) Dependency of emission intensity on the wavelength of the excitation laser. The measured intensity is normalized with the input power of the excitation laser with different wavelengths.

defect is preferentially generated on the surface of 2D h-BN. Therefore, the thickness of h-BN will largely influence the EF since the electric field intensity decays exponentially from the surface of plasmonic nanostructure. This phenomenon is theoretically investigated in detail in Appendix D. Experimental validation involves about 50 h-BN samples with varying thicknesses coupled to identical metasurfaces. Different thicknesses of h-BN will result in the shift of resonant wavelength, leading to the mismatch with single-photon emission. In order to make reasonable comparison, polymethyl methacrylate (PMMA) is spin-coated on top of the hybrid samples. The coating thickness of PMMA is finely adjusted to match the resonant wavelength of every sample with the single-photon emission. As shown in Fig. 4(a), the obtained EF_{em} distribution is rather random due to the mismatch between the atomic defect site and emission hotspot (see Appendix D). Nevertheless, the fitted maximum EF_{em} values follow an exponential decay trend above 7 nm thickness, aligning well with theoretical predictions. Below this threshold, the quenching effect dominates, which reduces emission efficiency. A maximum value of ∼154 for the EF_{em} is experimentally obtained when the thickness of h-BN is ∼7.4 nm.

The EF of single-photon emission can be further increased if both the emission and excitation wavelengths are in parallel with two resonant modes in the integrated system, respectively. When the excitation wavelength corresponds to the higher-order resonant modes in shorter wavelengths, the created double-resonance scheme will bring additional enhancement to single-photon emission. These higher order modes are indicated by multiple reflection dips around 500 nm, as shown in Figs. 3(a) and 3(b). In experiment, a pulsed laser system with broadband tunable wavelength (Sec. 1 of Supplemental Material [37]) is utilized to excite the sample with highest EF_{em} in Fig. 4(a) (thickness ∼7.4 nm), and emitted RCP signals are collected. As shown in Fig. 4(b), the maximum value of emission intensity appears at around 508 nm, corresponding to the 3rd-order anapole state [Figs. 3(a) and 3(b)]. In this manner, an additional excitation EF of ∼6.07 can be obtained, further improving the brightness of single-photon emission. Note that, the total enhancement is the product of emission and excitation enhancement, thus by comparing the emission intensity at 508 nm with that at 532 nm in Fig. 4(b), a total EF of ∼934 can be estimated.

Conclusions—We have demonstrated both considerable enhancement and comprehensive performance improvement of single-photon emission, in which anapole states and quasi-BICs are invoked. The maximum field intensity takes place when the radiative loss is equal to the dissipative loss, manipulated by the structural asymmetry. Increasing the gap size, the proportion of higher-order electric multipoles rises and EM energy is more highly confined in the near field, bringing immense field enhancement. Moreover, by breaking in-plane mirror symmetry, BIC can be formed for specific circular polarization, leading to single-photon emission with strong chirality. Substantial advances can be envisioned in quantum technologies in terms of excellent overall performance of single-photon sources. Our proposed EM enhancement mechanism can also be extended to other application scenarios requiring strong light-matter interaction.

Acknowledgments—This work was supported by the National Key R&D Program of China (No. 2022YFA1405004, No. 2022YFA1404800, and No. 2023YFA1406603), the National Natural Science Foundation of China (No. 11274159, No. 11374150, No. T2394473, and No. 12374112), and the Natural Science Foundation of Jiangsu Province, Major Project (No. BK20212004).

Data availability—The data that support the findings of this article are not publicly available upon publication because it is not technically feasible and/or the cost of preparing, depositing, and hosting the data would be prohibitive within the terms of this research project. The data are available from the authors upon reasonable request.

[1] Y. Kan and S. I. Bozhevolnyi, Advances in metaphotonics empowered single photon emission, Adv. Opt. Mater. **11**, 2202759 (2023).

[2] M. Esmann, S. C. Wein, and C. Antón-Solanas, Solid-state single-photon sources: Recent advances for novel quantum materials, Adv. Funct. Mater. **34**, 2315936 (2024).

[3] C. Kurtsiefer, S. Mayer, P. Zarda, and H. Weinfurter, Stable solid-state source of single photons, Phys. Rev. Lett. **85**, 290 (2000).

[4] Y. Arakawa and M. J. Holmes, Progress in quantum-dot single photon sources for quantum information technologies:

A broad spectrum overview, Appl. Phys. Rev. **7**, 021309 (2020).

[5] M. D'Amato, Q. Y. Tan, Q. Glorieux, A. Bramati, and C. Soci, Color-tunable mixed-cation perovskite single photon emitters, ACS Photonics **10**, 197 (2023).

[6] M. Turunen, M. Brotons-Gisbert, Y. Dai, Y. Wang, E. Scerri, C. Bonato, K. D. Jöns, Z. Sun, and B. D. Gerardot, Quantum photonics with layered 2D materials, Nat. Rev. Phys. **4**, 219 (2022).

[7] C. Wang, F. Yang, and Y. Gao, The highly-efficient light-emitting diodes based on transition metal dichalcogenides: From architecture to performance, Nanoscale Adv. **2**, 4323 (2020).

[8] C. Zhang, Z. Shi, T. Wu, and X. Xie, Microstructure engineering of hexagonal boron nitride for single-photon emitter applications, Adv. Opt. Mater. **10**, 2200207 (2022).

[9] N. Mendelson *et al.*, Identifying carbon as the source of visible single-photon emission from hexagonal boron nitride, Nat. Mater. **20**, 321 (2021).

[10] N. R. Jungwirth and G. D. Fuchs, Optical absorption and emission mechanisms of single defects in hexagonal boron nitride, Phys. Rev. Lett. **119**, 057401 (2017).

[11] N. Nikolay, N. Mendelson, E. Özelci, B. Sontheimer, F. Böhm, G. Kewes, M. Toth, I. Aharonovich, and O. Benson, Direct measurement of quantum efficiency of single-photon emitters in hexagonal boron nitride, Optica **6**, 1084 (2019).

[12] G. Noh, D. Choi, J.-H. Kim, D.-G. Im, Y.-H. Kim, H. Seo, and J. Lee, Stark tuning of single-photon emitters in hexagonal boron nitride, Nano Lett. **18**, 4710 (2018).

[13] P. G. Zotev *et al.*, Van der Waals materials for applications in nanophotonics, Laser Photonics Rev. **17**, 2200957 (2023).

[14] C. Li *et al.*, Arbitrarily structured quantum emission with a multifunctional metalens, eLight **3**, 19 (2023).

[15] T. T. H. Do, M. Nonahal, C. Li, V. Valuckas, H. H. Tan, A. I. Kuznetsov, H. S. Nguyen, I. Aharonovich, and S. T. Ha, Room-temperature strong coupling in a single-photon emitter-metasurface system, Nat. Commun. **15**, 2281 (2024).

[16] S. Cao, Y. Jin, H. Dong, T. Guo, J. He, and S. He, Enhancing single photon emission through quasi-bound states in the continuum of monolithic hexagonal boron nitride metasurface, J. Nonlinear Opt. Phys. Mater. **4**, 035001 (2021).

[17] F. Peyskens, C. Chakraborty, M. Muneeb, D. Van Thourhout, and D. Englund, Integration of single photon emitters in 2D layered materials with a silicon nitride photonic chip, Nat. Commun. **10**, 4435 (2019).

[18] J. E. Fröch, S. Kim, N. Mendelson, M. Kianinia, M. Toth, and I. Aharonovich, Coupling hexagonal boron nitride quantum emitters to photonic crystal cavities, ACS Nano **14**, 7085 (2020).

[19] S. Häußler, G. Bayer, R. Waltrich, N. Mendelson, C. Li, D. Hunger, I. Aharonovich, and A. Kubanek, Tunable fiber-cavity enhanced photon emission from defect centers in hBN, Adv. Opt. Mater. **9**, 2002218 (2021).

[20] K. Parto, S. I. Azzam, N. Lewis, S. D. Patel, S. Umezawa, K. Watanabe, T. Taniguchi, and G. Moody, Cavity-enhanced 2D material quantum emitters deterministically integrated with silicon nitride microresonators, Nano Lett. **22**, 9748 (2022).

[21] C. A. Chen, P. H. Chen, Y. X. Zheng, C. H. Chen, M. K. Hsu, K. C. Hsu, Y. Y. Lai, C. S. Chuu, H. Deng, and Y. H. Lee, Tunable single-photon emission with wafer-scale plasmonic array, Nano Lett. **24**, 3395 (2024).

[22] A. González-Tudela, A. Reiserer, J. J. García-Ripoll, and F. J. García-Vidal, Light-matter interactions in quantum nanophotonic devices, Nat. Rev. Phys. **6**, 166 (2024).

[23] F. Benz *et al.*, Single-molecule optomechanics in "picocavities," Science **354**, 726 (2016).

[24] K. J. Savage, M. M. Hawkeye, R. Esteban, A. G. Borisov, J. Aizpurua, and J. J. Baumberg, Revealing the quantum regime in tunnelling plasmonics, Nature (London) **491**, 574 (2012).

[25] T. Grange, G. Hornecker, D. Hunger, J.-P. Poizat, J.-M. Gérard, P. Senellart, and A. Auffèves, Cavity-funneled generation of indistinguishable single photons from strongly dissipative quantum emitters, Phys. Rev. Lett. **114**, 193601 (2015).

[26] A. E. Miroshnichenko, A. B. Evlyukhin, Y. F. Yu, R. M. Bakker, A. Chipouline, A. I. Kuznetsov, B. Luk'yanchuk, B. N. Chichkov, and Y. S. Kivshar, Nonradiating anapole modes in dielectric nanoparticles, Nat. Commun. **6**, 8069 (2015).

[27] C. W. Hsu, B. Zhen, A. D. Stone, J. D. Joannopoulos, and M. Soljačić, Bound states in the continuum, Nat. Rev. Mater. **1**, 16048 (2016).

[28] Q. H. Zhang, K. Liu, K. Qin, S. J. Fu, J. Du, Y. Q. Lu, Y. Y. Zhu, Y. F. Chen, and X. J. Zhang, Electromagnetic Raman enhancement beyond gap limit, Phys. Rev. Lett. **134**, 136902 (2025).

[29] Y. Yang, V. A. Zenin, and S. I. Bozhevolnyi, Anapole-assisted strong field enhancement in individual all-dielectric nanostructures, ACS Photonics **5**, 1960 (2018).

[30] S. I. Azzam and A. V. Kildishev, Photonic bound states in the continuum: From basics to applications, Adv. Opt. Mater. **9**, 2001469 (2021).

[31] Z. Sadrieva, K. Frizyuk, M. Petrov, Y. Kivshar, and A. Bogdanov, Multipolar origin of bound states in the continuum, Phys. Rev. B **100**, 115303 (2019).

[32] P. Hu, J. Wang, Q. Jiang, J. Wang, L. Shi, D. Han, Z. Q. Zhang, C. T. Chan, and J. Zi, Global phase diagram of bound states in the continuum, Optica **9**, 1353 (2022).

[33] Y. Zhang, A. Chen, W. Liu, C. W. Hsu, B. Wang, F. Guan, X. Liu, L. Shi, L. Lu, and J. Zi, Observation of polarization vortices in momentum space, Phys. Rev. Lett. **120**, 186103 (2018).

[34] Y. Chen *et al.*, Observation of intrinsic chiral bound states in the continuum, Nature (London) **613**, 474 (2023).

[35] T. Shi *et al.*, Planar chiral metasurfaces with maximal and tunable chiroptical response driven by bound states in the continuum, Nat. Commun. **13**, 4111 (2022).

[36] I. Gontijo, M. Boroditsky, E. Yablonovitch, S. Keller, U. K. Mishra, and S. P. DenBaars, Coupling of InGaN quantum-well photoluminescence to silver surface plasmons, Phys. Rev. B **60**, 11564 (1999).

[37] See Supplemental Material at http://link.aps.org/supplemental/10.1103/kf83-1b8s, which includes Refs. [38–49], for details on methods, measured dielectric function of single-crystalline Ag, the period of metasurface, calculation on emission enhancement, multipole decomposition, emitter-cavity coupling theory, near-field measurements, time correlation measurements, correction of second-order correlation function,

chirality of the metasurface, and statistical distribution of emission enhancement.

[38] H. Ditlbacher, A. Hohenau, D. Wagner, U. Kreibig, M. Rogers, F. Hofer, F. R. Aussenegg, and J. R. Krenn, Silver nanowires as surface plasmon resonators, Phys. Rev. Lett. **95**, 257403 (2005).

[39] H. Jiang, L. Mao, K. Jiang, C. Liu, D. Zhang, Y. Lu, P. Wang, and H. Ming, Local spectroscopy of silver nanowire in different environments excited with a halogen lamp, Opt. Lett. **39**, 4707 (2014).

[40] A. Garcia-Etxarri, I. Romero, F. J. Garcia de Abajo, R. Hillenbrand, and J. Aizpurua, Influence of the tip in near-field imaging of nanoparticle plasmonic modes: Weak and strong coupling regimes, Phys. Rev. B **79**, 125439 (2009).

[41] P. Alonso-González *et al.*, Resolving the electromagnetic mechanism of surface-enhanced light scattering at single hot spots, Nat. Commun. **3**, 684 (2012).

[42] P. B. Johnson and R. W. Christy, Optical constants of the noble metals, Phys. Rev. B **6**, 4370 (1972).

[43] E. Petryayeva and U. J. Krull, Localized surface plasmon resonance: Nanostructures, bioassays and biosensing—A review, Anal. Chim. Acta **706**, 8 (2011).

[44] Y. Liang, D. P. Tsai, and Y. Kivshar, From local to nonlocal high-Q plasmonic metasurfaces, Phys. Rev. Lett. **133**, 053801 (2024).

[45] Y. Yuan *et al.*, Robust Purcell effect of $CsPbI_3$ quantum dots using nonlocal plasmonic metasurfaces, Phys. Rev. Lett. **134**, 243804 (2025).

[46] M. H. Tahersima *et al.*, Testbeds for transition metal dichalcogenide photonics: Efficacy of light emission enhancement in monomer vs dimer nanoscale antennae, ACS Photonics **4**, 1713 (2017).

[47] G. Liu, W. Zhou, D. Gromyko, D. Huang, Z. Dong, R. Liu, J. Zhu, J. Liu, C.-W. Qiu, and L. Wu, Single-photon generation and manipulation in quantum nanophotonics, Appl. Phys. Rev. **12**, 011308 (2025).

[48] T. Neuman, P. Alonso-González, A. Garcia-Etxarri, M. Schnell, R. Hillenbrand, and J. Aizpurua, Mapping the near fields of plasmonic nanoantennas by scattering-type scanning near-field optical microscopy, Laser Photonics Rev. **9**, 637 (2015).

[49] R. Hanbury Brown and R. Q. Twiss, Correlation between photons in two coherent beams of light, Nature (London) **177**, 27 (1956).

[50] C. Y. Wang, H. Y. Chen, L. Sun, W. L. Chen, Y. M. Chang, H. Ahn, X. Li, and S. Gwo, Giant colloidal silver crystals for low-loss linear and nonlinear plasmonics, Nat. Commun. **6**, 7734 (2015).

[51] K. Qin, K. Liu, S. Peng, Z. Y. Zuo, X. He, J. P. Ding, Y. Q. Lu, Y. Y. Zhu, and X. J. Zhang, Strongly coupled Raman scattering enhancement revealed by scattering-type scanning near-field optical microscopy, Nanophotonics **12**, 1857 (2023).

[52] S. A. Maier, Plasmonic field enhancement and SERS in the effective mode volume picture, Opt. Express **14**, 1957 (2006).

[53] N. Bernhardt, K. Koshelev, S. J. U. White, K. W. C. Meng, J. E. Fröch, S. Kim, T. T. Tran, D. Y. Choi, Y. Kivshar, and A. S. Solntsev, Quasi-BIC resonant enhancement of second-harmonic generation in WS_2 monolayers, Nano Lett. **20**, 5309 (2020).

[54] P. Grahn, A. Shevchenko, and M. Kaivola, Electromagnetic multipole theory for optical nanomaterials, New J. Phys. **14**, 093033 (2012).

[55] E. A. Gurvitz, K. S. Ladutenko, P. A. Dergachev, A. B. Evlyukhin, A. E. Miroshnichenko, and A. S. Shalin, The high-order toroidal moments and anapole states in all-dielectric photonics, Laser Photonics Rev. **13**, 1800266 (2019).

[56] Q. H. Zhang, K. Liu, S. J. Fu, X. H. Hong, C. Zhang, Y. Q. Lu, Y. Y. Zhu, Y. F. Chen, and X. J. Zhang, Boosting optical nonlinearity of van der Waals materials with high-order multipoles, Laser Photonics Rev. **19**, 2401850 (2025).

[57] R. E. K. Fishman, R. N. Patel, D. A. Hopper, T.-Y. Huang, and L. C. Bassett, Photon-emission-correlation spectroscopy as an analytical tool for solid-state quantum defects, PRX Quantum **4**, 010202 (2023).

End Matter

Appendix A: Field distribution of the resonant modes—The sharp corners in the cruciform structure support GPP mode under x-polarized input light. The charge distribution and multipole moments of this mode are drawn according to the EM field distribution in Fig. 5(a). On the metal-air interface, the E_z distribution effectively maps the surface charge accumulation, thus establishing the orientation of the ED moment. Similarly, the spatial distribution of H_z reveals the opposing magnetic fields at the ends of the groove, directly illustrating the formation of a magnetic loop. This loop is the signature of the TD moment, confirming its role in forming the anapole state. More detailed discussion on spatial orientations of the multipoles can be found in Sec. 5 of Supplemental Material [37].

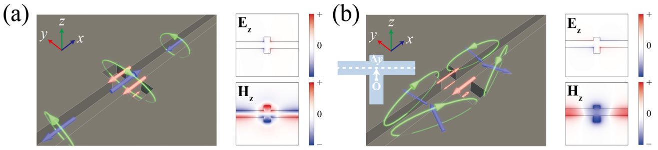

FIG. 5. Field distribution of the resonant modes. (a),(b) Multipole moments and field distributions of the optical modes in symmetric cruciform structure (a) and asymmetric cruciform structure (b). The red, blue, and green arrows stand for ED, TD, and MD moments, respectively.

When the symmetry along the y direction is broken by shifting the horizontal groove Δy from origin [Fig. 5(b)], an extra quasi-BIC which possesses antisymmetric electric field distribution can be excited from far field. By comparison to the mode of symmetric structure [Fig. 5(a)], there is a lack of TD moments located in the vertical groove and mainly antisymmetric distributions of ED and TD moments for the quasi-BICs of asymmetric structure [Fig. 5(b)], creating higher-order multipole moments.

Appendix B: Far-field characteristics of experimental samples—Figure 6(a) shows the optical micrograph of the h-BN sample with thicknesses of ∼25 nm. To characterize the defect site, the sample is excited by 532 nm continuous-wave laser and spatially scanned with a step size of 200 nm. The light emission mapping, as well as the spectrum, is also shown in Fig. 6(a). Single-photon emission is observed at the wavelength around 580 nm with narrow full width at half-maximum of several nanometers, which corresponds with the ZPL [9]. An extra peak with broader linewidth at around 630 nm, i.e., the PSB [9] is also obtained, in accord with the characteristics of the carbon-related defect in h-BN.

As for the metasurface, the calculated dispersion relation of the fabricated structure is mapped by the angle-resolved reflection spectra in Fig. 6(b), which is in good agreement with the experimental one. The dispersion relation exhibits zero group velocity ($v_g = \mathrm{d}\omega/\mathrm{d}k$) at the Γ point, indicating the localized feature. Then the h-BN sample in Fig. 6(a) is transferred to couple with the metasurface by dry-transfer method. The dispersion relations are measured again for the same sample, as shown in Fig. 6(c). The consistency between experimental and theoretical results is confirmed again, and the difference in resonant wavelengths of Figs. 6(b) and 6(c) is induced by the high refractive index of h-BN. The sample with specific thickness exactly resonates at around 580 nm, in correspondence with the emission wavelength of single-photon emission. Although far-field measurement results show good consistency with calculated ones, check on the near-field distribution of the optical mode is needed to verify the fabricated structure. Scattering-type scanning near-field optical microscopy (s-SNOM) is used to measure the field distribution at resonant wavelengths of the bare metasurface and that coupled with h-BN, as shown in Sec. 7 of Supplemental Material [37]. The measured electric field distribution is in line with the calculated one, providing direct evidence of local field enhancement.

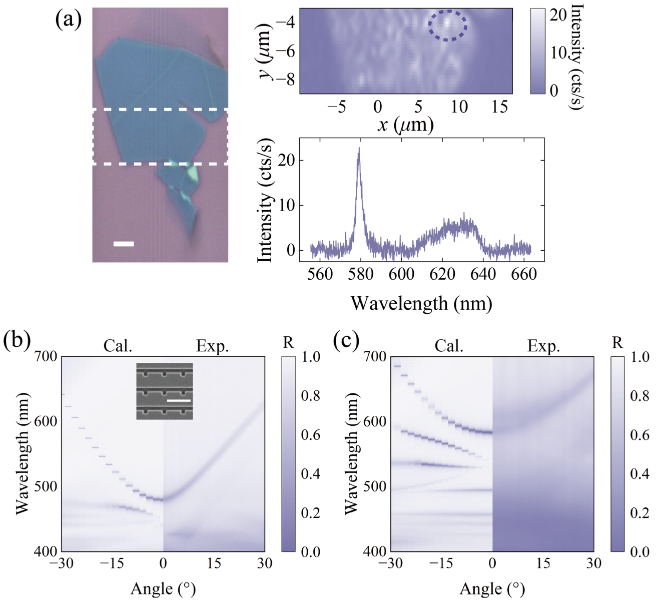

FIG. 6. Far-field characteristics of the experimental samples. (a) Optical micrographs (scale bar, 5 μm), scanning images and emission spectrum of h-BN sample with the thickness of ∼25 nm. The scanning image is obtained by mapping the peak intensity in the wavelength range of 570–590 nm. The rectangle on the micrograph indicates the scanned area, and the circle on the scanning image indicates the atomic defect site. (b),(c) Calculated and measured dispersion relations for the bare metasurface without h-BN (b) and metasurface coupled with the h-BN sample (c). The structural parameters are $L = 100$, $w = 80$, $h = 30$, $P = 400$, and $\Delta y = 60$ nm. The inset in the measured dispersion relation is the scanning electron microscope image of the fabricated structure (scale bar, 500 nm).

Appendix C: Characteristics of the chiral configuration—The bare chiral metasurface without coupling with h-BN is characterized in Sec. 10 of Supplemental Material [37], where measured results match well with calculated ones, confirming the accuracy of fabrication. For the defective h-BN integrated with the metasurface, the resonant wavelength of the metasurface will shift and match with that of single-photon emission when the thickness of h-BN is ∼18 nm. Angle-resolved reflection spectra are measured for

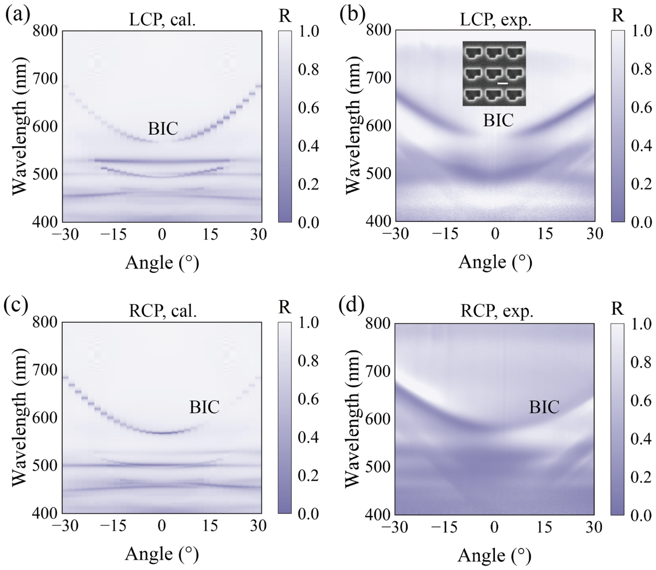

FIG. 7. Angle-resolved white-light reflection spectra of the integrated system. (a),(b) Calculated (a) and measured (b) angle-resolved white light reflection spectra for the LCP. The inset is the scanning electron microscope image of fabricated chiral metasurface. Scale bar, 200 nm. (c),(d) Calculated (c) and measured (d) angle-resolved white light reflection spectra for the RCP.

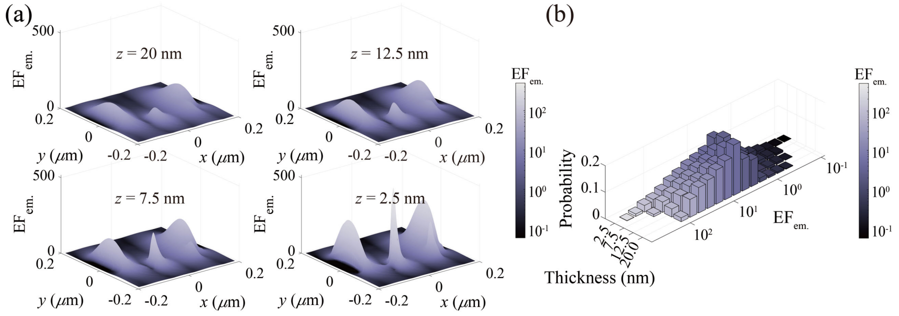

FIG. 8. Dependency of emission intensity on the spatial position of the single-photon emitter. (a) Calculated EF_{em} with different spatial position of the atomic defect within a period. In the numerical calculation, atomic defect is simplified as a point dipole source since it can be considered dimensionless when compared with the size of the metasurface period. (b) Calculated probability histogram of EF_{em} of the metasurface with different thickness of h-BN.

different circular polarizations, in which the hybrid sample is excited with LCP and RCP white light and the reflected signals of all polarizations are collected. For the LCP [Figs. 7(a) and 7(b)], the BIC point can be observed at the Γ point in momentum space. While for the RCP [Figs. 7(c) and 7(d)], the BIC point is off from the Γ point by about 15° and resonant mode will be excited with incident light in the normal direction. It can be seen that the experimental results are in agreement with simulated ones, verifying the validity of our theory.

Appendix D: Dependency of emission intensity on spatial position of emitter—To investigate the influence of the h-BN thickness on the single-photon emission, the EF_{em} is calculated with different spatial position of the atomic defect in Fig. 8(a). The results demonstrate that the emission hotspot intensifies and sharpens as the atomic defect approaches the plasmonic surface, consistent with the evanescent wave's exponential decay profile. Figure 8(a) also reveals significant in-plane positional dependence of EF_{em}. This spatial sensitivity presents a statistical distribution of actual EF_{em} due to random defect placement within the plane. By calculating the emission hotspot area (Sec. 11 of Supplemental Material [37]), Fig. 8(b) quantifies this behavior through probability histograms at different z positions. Near-surface defects exhibit higher maximum EFs but low occurrence probabilities. Most EF_{em} values cluster in the $10^1 - 10^2$ range, which is achievable through limited experimental repetitions.